

---

# DiViNeT: 3D Reconstruction from Disparate Views via Neural Template Regularization

---

Aditya Vora<sup>1</sup> Akshay Gadi Patil<sup>1</sup> Hao Zhang<sup>1,2</sup>

<sup>1</sup>Simon Fraser University      <sup>2</sup>Amazon

## Abstract

We present a volume rendering-based neural surface reconstruction method that takes as few as three *disparate* RGB images as input. Our key idea is to regularize the reconstruction, which is severely ill-posed and leaving significant gaps between the sparse views, by learning a set of *neural templates* to act as surface priors. Our method, coined DiViNet, operates in two stages. It first learns the templates, in the form of 3D Gaussian functions, across different scenes, without 3D supervision. In the reconstruction stage, our predicted templates serve as anchors to help “stitch” the surfaces over sparse regions. We demonstrate that our approach is not only able to complete the surface geometry but also reconstructs surface details to a reasonable extent from a few disparate input views. On the DTU and BlendedMVS datasets, our approach achieves the best reconstruction quality among existing methods in the presence of such sparse views and performs on par, if not better, with competing methods when dense views are employed as inputs. Project Page: <https://aditya-vora.github.io/divinetpp/>.

## 1 Introduction

3D reconstruction from multi-view images is a fundamental task in computer vision. Recently, with the rapid advances in neural fields [55, 34] and differentiable rendering [20], many methods have been developed for neural 3D reconstruction [37, 60, 26, 31, 51, 25, 59, 39, 67, 54]. Among them, volume rendering-based methods have achieved impressive results. Exemplified by neural radiance fields (NeRF) [34], these approaches typically employ compact MLPs to encode scene geometry and appearance, with network training subjected to volume rendering losses in RGB space.

The main drawback of most of these methods is the requirement of dense views with considerable image overlap, which may be impractical in real-world settings. When the input views are sparse, these methods often fail to reconstruct accurate geometries due to radiance ambiguity [66, 53]. Despite employing smoothness priors during SDF/occupancy prediction as an inductive bias [37, 60, 51, 59], the limited overlap between regions in the input images causes little-to-no correlation to the actual 3D surface, resulting in holes and distortions, among other artifacts, in the reconstruction.

Several recent attempts have been made on neural reconstruction from sparse views. SparseNeuS [28] learns generalizable priors across scenes by constructing geometry encoding volumes at two resolutions in a coarse-to-fine and cascading manner. While the method can handle as few as 2 or 3 input images, the corresponding views must be sufficiently close to ensure significant image overlap and quality reconstruction. MonoSDF [63] relaxes on the image overlap requirement and relies on geometric monocular priors such as depth and normal cues to boost sparse-view reconstruction. However, such cues are not always easy to obtain, e.g., MonoSDF relied on a pre-trained depth estimation model requiring 3D ground-truth (GT) data. Moreover, depth prediction networks often rely on cost volumes [57, 15] which are memory expensive and thus restricted to predicting low-resolution depth maps. Because of this, the results obtained typically lack fine geometric details [63].

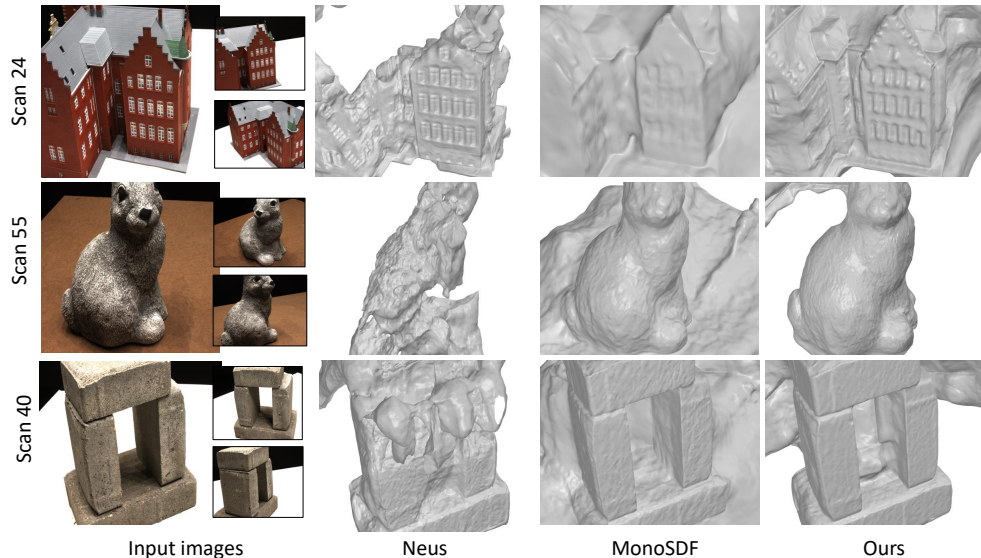


Figure 1: Surface reconstruction results on the DTU dataset [18] for three disparate view inputs (shown on the left). We compare our technique against NeuS[51], which does not use any regularization, and against MonoSDF [63], which uses additional depth and normal supervision to regularize the surface reconstruction process. The results clearly show that our method not only reconstructs the complete surface but also preserves sharp geometric details *without* using any other ground truth information beyond the RGB inputs. See Section 4.1 for a detailed explanation.

In this paper, we target neural surface reconstruction from sparse *and disparate* views. That is, not only are the input RGB images few in number, they also do not share significant overlap; see Figure 1. Our key idea is to regularize the reconstruction, which is severely ill-posed and leaves significant gaps to be filled in between the few disparate views, by learning a set of *neural templates* that act as surface priors. Specifically, in the first stage, we learn the neural templates, in the form of 3D Gaussian functions, across different scenes. Our network is a feedforward CNN encoder-decoder, trained with RGB reconstruction and auxiliary losses against the input image collection. In the second stage, surface reconstruction via volume rendering, our predicted templates serve as anchors to help “stitch” the surfaces over sparse regions without negatively impacting the ability of the signed distance function (SDF) prediction network from recovering accurate geometries.

Our two-stage learning framework (see Figure 2) is coined DiViNet for neural 3D reconstruction from Disparate Views via NEural Templates regularization. We conduct extensive experiments on two real-world object-scenes datasets, viz., DTU [18] and BlendedMVS [58], to show the efficiency of our method over existing approaches on the surface reconstruction task, for both sparse and dense view input settings. Through ablation studies, we validate the design choices of our network in the context of different optimization constraints employed during training.

## 2 Related Work

**View-based 3D Reconstruction.** Reconstructing 3D surfaces from image inputs is a non-trivial task mainly due to the difficulty of establishing reliable correspondences between different regions in the input images and estimating their correlation to the 3D space. This is especially pronounced when the number of views is *limited* and *disparate*. Multi-view stereo (MVS) techniques, both classical [1, 3, 7, 10, 47, 13, 4, 44, 48], and learning-based [30, 50, 64, 42, 17, 57, 62], while using an explicit 3D representation, address the problem of multi-view 3D reconstruction either by estimating depth via feature matching across different input views or by voxelizing 3D space for shape reconstruction.

A recent exploration of neural implicit functions for 3D shape/scene representation [32, 40, 33, 27, 49, 43, 19] has led to an explosion of 3D reconstruction from multi-view images, where two prominent directions exist – one based on surface rendering techniques [37, 60, 26], which require accurate 2D masks at the input, and the other based on volume rendering techniques [31, 51, 25, 59, 39, 67, 54],

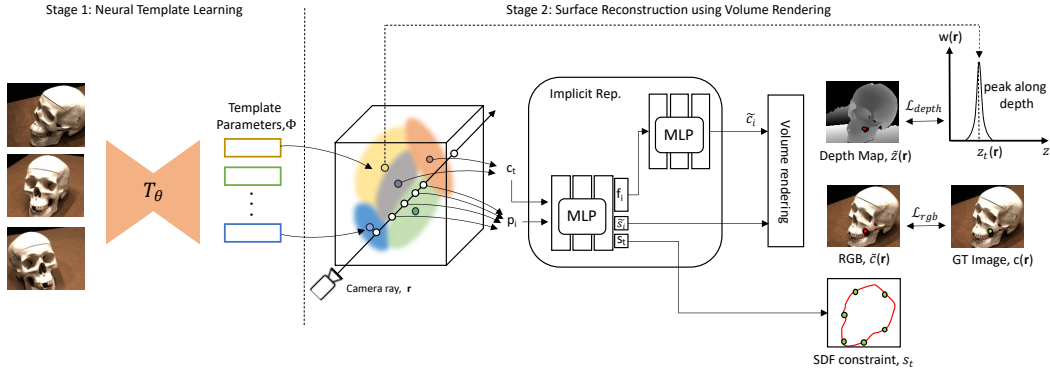


Figure 2: A two-stage learning framework developed to reconstruct 3D surfaces from sparse, disparate view input images. In Stage 1 (see Section 3.1), we train a network across different scenes to predict structured templates (Gaussians, in our case) that encode surface priors. In Stage 2 (see Section 3.2), we train a surface reconstruction model to reconstruct the surface SDF values by leveraging the predicted templates from Stage 1. The purpose served by the predicted templates is in aiding the reconstruction process by acting as regularizers, allowing to obtain complete geometry (see Figure 1 and 7), and even details to a reasonable extent (see Figure 5), from disparate view inputs.

which require no such object masks. The latter techniques combine the representational power of neural implicit with the recently proposed NeRF models [34], achieving better surface reconstructions over the former techniques. A major drawback of these works is that they all require *dense* multi-view images as input. Two recent techniques, Sparse NeUS [28] and Mono-SDF [63] learn 3D reconstruction from just three input images. In the case of [28], the three input images have a significant amount of overlap, and can not be employed when the views are disparate. [63], on the other hand, leverages additional cues such as ground truth depths and normals, allowing reconstruction from disparate views. Our work differs from these in the sense that we do not make use of any explicit cues in the form of ground truth depths and normals, while still being able to faithfully reconstruct 3D surfaces from just three disparate RGB images as input.

**Regularizing Neural Surface Reconstruction.** Our ability to reconstruct 3D surfaces from sparse, disparate view images is made possible through template-based regularization that provides helpful surface priors during the volume rendering stage. Regularization has been explored in the context of novel-view synthesis [36, 8], where patch-based regularization for both the scene geometry and color is performed [36] or additional cues such as depth supervision are incorporated [8] while handling sparse inputs in both cases. In the context of surface reconstruction, MonoSDF [63] uses depth and normal supervision as a part of unsaid regularization to obtain surface geometry from sparse input images. Other works [6, 65, 9] study the effect of regularization on the volumetric rendering-based surface reconstruction framework. Their goal is to improve surface reconstruction by imposing multi-view photometric and COLMAP [46] constraints on the Signed Distance Field (SDF) prediction during training. Such methods show significant improvements over vanilla approaches for surface reconstruction. However, under sparse scenarios, because of significant view differences, photometric and COLMAP constraints are difficult to satisfy, resulting in poor reconstruction quality. In contrast to these methods, inspired by [12, 11, 38], we propose to learn surface priors in the form of templates across a data distribution and use these templates to guide the reconstruction process.

### 3 Method

Our method achieves 3D reconstruction of solid objects from a small set of RGB images  $\{I_i\}_{i=0}^{N-1}$  with very less visual overlap, where  $N$  can be as less as 3 images and  $I_i \in [0, 1]^{H \times W \times 3}$ . We assume that camera extrinsics and intrinsics are known for all the images. As shown in Figure 2 our approach is realized in two stages: (1) Learning a network for predicting shape templates (see Section 3.1), and (2) Leveraging the predicted templates, learning a volumetric surface reconstruction network with depth and SDF constraints (see Section 3.2).

### 3.1 Stage 1: Learning Surface Priors with Neural Templates

**Template Representation.** We represent the shape with a bunch of  $N_t$  local implicit functions called templates, where the influence of  $i^{th}$  template is represented as  $g_i(p, \varphi_i)$  and is given by,

$$g_i(p, \varphi_i) = s_i \exp \left( \sum_{d \in \{x, y, z\}} \frac{-(c_{i,d} - p_d)^2}{2r_{i,d}^2} \right), \quad (1)$$

where  $p \in \mathbb{R}^3$  is the 3D location of a point in the volume and  $\varphi_i$  is the template parameter. Specifically, each template  $\varphi_i$  is represented as a scaled, anisotropic 3D Gaussian,  $\varphi_i \in \mathbb{R}^7$ , which consists of a scaling factor  $s_i$ , a center point  $c_i \in \mathbb{R}^3$ , and per-axis radii  $r_i \in \mathbb{R}^3$ . Using this local implicit function, we can find the probability of a point near the surface by summing up the influences of all  $N_t$  templates, i.e.  $G(p, \Phi) = \sum_{i=1}^{N_t} g_i(p, \varphi_i)$ , where  $\Phi$  is the set of all the template parameters.

**Network Architecture.** Figure 3 shows the template training stage. Given a fixed set of  $N_t$  templates ( $\Phi$ ) and input images set  $\{I_i\}$ , we aim to optimize a network  $\mathcal{T}_\theta$  for the task of template prediction which comprises of an encoder ( $\mathcal{E}$ ) and decoders ( $\mathcal{D}_{geo}, \mathcal{D}_{vox}$ ). The encoder is a feed-forward Convolutional Neural Network (CNN), which we first use to extract 2D image features from individual input views. We then obtain per template latent code  $z_{\varphi_i} \in \mathbb{R}^{64}$  using a bi-linear interpolation step as shown in Figure 4. For this step, depending on the number of templates, we create a uniform grid of points, which we then use for the interpolation of features obtained from convolutional layers. Each latent code of the template,  $z_{\varphi_i}$  is then decoded through two decoders  $\mathcal{D}_{geo}$  and  $\mathcal{D}_{vox}$ .  $\mathcal{D}_{geo}$  is the geometry decoder with simple MLP layers predicting the template parameters  $\varphi_i$ . That is,  $\mathcal{D}_{geo} : \mathbb{R}^{64} \rightarrow \mathbb{R}^7$ .  $\mathcal{D}_{vox}$ , on the other hand, is a feature decoder comprised of transposed convolutional layers. The objective of  $\mathcal{D}_{vox}$  is to map the template feature representation,  $z_{\varphi_i}$ , to a local volumetric feature grid for each individual template.

Decoding all the template latent codes  $z_{\varphi_i}$  at once through  $\mathcal{D}_{vox}$  results in a dense voxel grid  $V \in \mathbb{R}^{(C * \mathcal{M}) \times (\mathcal{M} * \sqrt{N_t}) \times (\mathcal{M} * \sqrt{N_t})}$ , which we then rearrange to  $N_t$  local volumes of size  $\mathbb{R}^{C \times \mathcal{M}^3}$ , where  $C$  is the feature dimension of each voxel and  $\mathcal{M}$  is the resolution of the feature grid. In our experiments, we set  $N_t = 576$ ,  $C = 8$  and  $\mathcal{M} = 16$ . For more details refer to supplementary.

**Network Training.** Due to the lack of ground truth 3D information of objects in the training set, we use RGB reconstruction loss along with auxiliary losses to optimize the template parameters. Given the predicted feature volume from the template network, we can query a continuous field at any 3D query point  $p_i$  by passing its tri-linearly interpolated feature  $f_{vox}(p_i)$ , along with the location  $p_i$  to a small MLP, consisting of 2 layers and 256 hidden dimensions. The output of the MLP is the color prediction at that particular query point,  $p_i$  in the 3D space. In addition to color, we compute each point’s blending weights  $w_i$  in 3D space using our predicted templates. This blending weight is computed by summing up the local influences of each template on the query point. We then integrate the predicted colors and weights to obtain the predicted image  $\hat{I}$ . For  $K$  query points sampled along a ray, this can be written as:

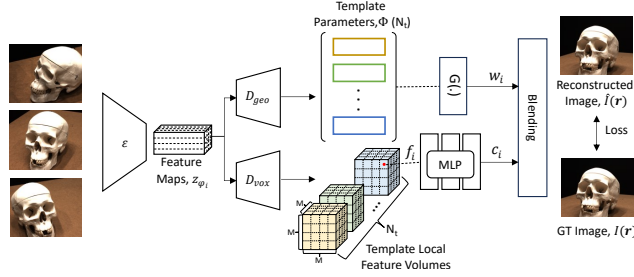


Figure 3: Template Learning stage. We train the template prediction network across scenes to predict  $N_t$  structured templates  $\Phi$ , alongwith local feature volumes per template.

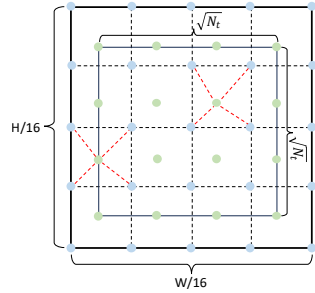


Figure 4: Interpolation step.  $\sqrt{N_t} \times \sqrt{N_t}$  codes obtained from  $H/16 \times W/16$  features.

$$\hat{I}(r) = \sum_{i=1}^K w_i c_i, \quad w_i = \frac{G(p_i, \Phi)}{\sum_i G(p_i, \Phi) + \epsilon} \quad (2)$$

Here,  $p_i$  is a query point along a ray,  $\epsilon$  is a small perturbation to prevent  $w_i$  from diverging to infinity when  $G(p_i, \Phi)$  takes small values, whereas  $G(p_i, \Phi) = \sum_{i \in N_t} g_i(p_i, \phi_i)$ . We then optimize our template prediction network using RGB reconstruction loss. To make sure that the predicted templates are plausible and near the surface, we propose auxiliary loss functions. The total loss by combining all the losses is given as:

$$\mathcal{L}_{total} = \mathcal{L}_{rgb} + \lambda_{cd} \mathcal{L}_{chamfer} + \lambda_c \mathcal{L}_{cov} + \lambda_r \mathcal{L}_{radius} + \lambda_v \mathcal{L}_{var} \quad (3)$$

Here,  $\mathcal{L}_{rgb}$  is the mean square error loss between the predicted pixel  $\hat{I}(\mathbf{r})$  and ground truth pixels  $I(\mathbf{r})$  which is defined as:

$$\mathcal{L}_{rgb} = \sum_{r \in \mathcal{R}} \|\hat{I}(r) - I(r)\|_2^2 \quad (4)$$

$\mathcal{L}_{chamfer}$  is the chamfer distance loss, which minimizes the distance between the template centers  $\{C_t : c_1, c_2, \dots, c_{N_t} \in \mathbb{R}^3\}$ , with the corresponding sparse reconstructed point cloud  $\{S_c : s_1, s_2, \dots, s_N \in \mathbb{R}^3\}$  obtained using triangulation, from COLMAP[46]. This loss makes sure that the predicted templates from the network are near the surface. This is given by:

$$\mathcal{L}_{chamfer} = \frac{1}{|C_t|} \sum_{c_i \in C_t} \min_{s_j \in S_c} (\|c_i - s_j\|_2^2) + \frac{1}{|S_c|} \sum_{s_j \in S_c} \min_{c_i \in C_t} (\|s_j - c_i\|_2^2) \quad (5)$$

$\mathcal{L}_{cov}$  is the coverage loss, which is defined over the entire sparse points,  $S_c$ . This ensures that the predicted templates cover the entire object. It is defined as,

$$\mathcal{L}_{cov} = \frac{1}{|S_c|} \sum_{s \in S_c} (1 - \sigma(\sum_{i=1}^{N_t} g_i(s, \varphi_i))) \quad (6)$$

where  $\sigma(\cdot)$  is the sigmoid function. In addition to this, we also use radius  $\mathcal{L}_{radius}$  and variance loss  $\mathcal{L}_{var}$ , which penalizes large and skewed template radii. This is given by:

$$\mathcal{L}_{radius} = \sum_{r_i \in R_t} \|r_i\|_2^2, \quad \mathcal{L}_{var} = \sum_{r_i \in R_t} \|r_i - \bar{r}_t\|^2 \quad (7)$$

Here,  $R_t$  is the set of all template radii.  $r_i$  is the individual template radii, and  $\bar{r}_t$  is the mean radius across all the templates,  $N_t$ .

### 3.2 Stage 2: Surface Reconstruction using Volume Rendering

**Geometry Representation and Volume Rendering.** Following the recent works of surface reconstruction with volume rendering [51, 59, 39], we represent the volume contained by the object to be reconstructed using a signed distance field  $\tilde{s}_i$ , which is parameterized using an MLP  $f_{\theta_s}$ , with learnable parameters  $\theta_s$  i.e  $\tilde{s}_i = f_{\theta_s}(\gamma(x_i))$ . Here  $\gamma(\cdot)$  is the positional encoding of point in 3D space [34]. Given the signed distance field, the surface  $\mathcal{S}$  of the object is represented as its zero-level set i.e.

$$\mathcal{S} = \{x \in \mathbb{R}^3 | f_{\theta_s}(x) = 0\}. \quad (8)$$

To train the SDF network in volume rendering framework, we follow [51], and use the below function, to convert the SDF predictions,  $f_{\theta_s}(p_i)$  to  $\alpha_i$  at each point,  $p_i$  in the 3D space.

$$\alpha_i = \max \left( \frac{\Phi_s(f_{\theta_s}(p_i)) - \Phi_s(f_{\theta_s}(p_{i+1}))}{\Phi_s(f_{\theta_s}(p_i))}, 0 \right). \quad (9)$$

Here,  $\Phi_s(x) = (1 + e^{-sx})^{-1}$  is the *sigmoid* function and  $s$  is learned during training.

Along with the signed distance field,  $\tilde{s}_i$ , we also predict color,  $\tilde{c}_i$  for each sampled point in 3D space using a color MLP,  $f_{\theta_c}$ . Following [60] the input to the color MLP is a 3D point  $p_i$ , a viewing

direction  $\hat{d}$ , analytical gradient  $\hat{n}_i$  of our SDF, and a feature vector  $z_i$  computed for each point  $p_i$  by  $f_{\theta_s}$ . Hence, the color MLP is the following function,  $\tilde{c}_i = f_{\theta_c}(p_i, \hat{d}, \hat{n}_i, z_i)$ . We optimize these networks using volume rendering, where the rendered color of each pixel is integrated over  $M$  discretely sampled points  $\{p_i = o + t_i \hat{d} | i = 1, \dots, M, t_i < t_{i+1}\}$  along a ray traced from camera center  $o$  and in direction  $\hat{d}$ . Following [34] the accumulated transmittance  $T_i$  for a sample point  $p_i$  is defined as  $T_i = \prod_{j=1}^{i-1} (1 - \alpha_j)$ , where  $\alpha_j$  is the opacity value defined in Eq. 9. Following this, we can compute the pixel color and depth as follows:

$$\hat{C}(r) = \sum_{i=1}^M T_i \alpha_i \tilde{c}_i, \quad \hat{z}(r) = \sum_{i=1}^M T_i \alpha_i t_i \quad (10)$$

**Optimization.** The overall loss function we use for optimizing for the surface is:

$$\mathcal{L} = \mathcal{L}_{color} + \lambda_1 \mathcal{L}_{eikonal} + \lambda_2 \mathcal{L}_{depth} + \lambda_3 \mathcal{L}_{sdf} \quad (11)$$

$\mathcal{L}_{color}$ , is the L1 loss between the predicted and ground truth colors which is given as:

$$\mathcal{L}_{color} = \sum_{r \in \mathcal{R}} \|\hat{C}(r) - C(r)\|_1 \quad (12)$$

Following [14] we use Eikonal loss to regularize the SDF in 3D space, which is given as:

$$\mathcal{L}_{eikonal} = \sum_{x \in \mathcal{X}} (\|\nabla f_{\theta_s}(x)\|_2 - 1)^2 \quad (13)$$

In addition to these, we propose the following regularization terms in order to aid the surface reconstruction process, especially in sparse reconstruction scenarios.

**Depth Loss:** We sample depth cues  $z_t(r)$  along each ray using the templates predicted by our template network. These depth cues are obtained by finding the depth locations where the template weight function  $w(x)$  at a point  $x$ , mentioned in 2 attains a maximum value among all the points sampled along a ray. We then minimize the L1 loss  $\mathcal{L}_{depth}$  between the predicted depth,  $\hat{z}(r)$  and the computed depth cues  $z_t(r)$  as:

$$\mathcal{L}_{depth} = \sum_{r \in \mathcal{R}_{valid}} \|\hat{z}(r) - z_t(r)\|_1 \quad (14)$$

Here,  $\mathcal{R}_{valid}$  denotes the set of rays that intersect the templates in the 3D space. We find these rays using ray sphere intersection.

**SDF Loss:** In addition to depth, we also constraint our SDF to pass through the template centers which we assume are near the surface. This is done by minimizing the L1 loss between the SDF at the template centers and the zero-level set. Here,  $N_t$  is the number of template parameters.

$$\mathcal{L}_{sdf} = \frac{1}{N_t} \sum_{x \in C_t} \|f_{\theta_s}(x)\|_1 \quad (15)$$

**Implementation Details.** Our implementation is based on the PyTorch framework [41]. For both stages, we use the Adam optimizer [22] to train our networks and set a learning rate of  $5e^{-4}$ . For stage-1, we set  $\lambda_{cd}$ ,  $\lambda_c$ ,  $\lambda_r$  and  $\lambda_v$  to 1.0, 0.1, 0.1, and 1.0, respectively. And for stage-2, we set  $\lambda_1$ ,  $\lambda_2$  and  $\lambda_3$  to 1.0, 0.8 and 0.8, respectively. As the templates are not perfect, we follow [63] and use an exponentially decaying loss weight for both SDF and depth regularization for the first  $25k$  iterations of optimization. During training in both stages, we sample a batch of 512 rays in each iteration. During both stages, we assume that the object is within the unit sphere. Our SDF network  $f_{\theta_s}$ , is an 8 layer MLP with 256 hidden units with a skip connection in the middle. The weights of the SDF network are initialized by geometric initialization [2]. The color MLP is a 4 layer MLP with 256 hidden units. The 3D position is encoded with 6 frequencies, whereas the viewing direction is

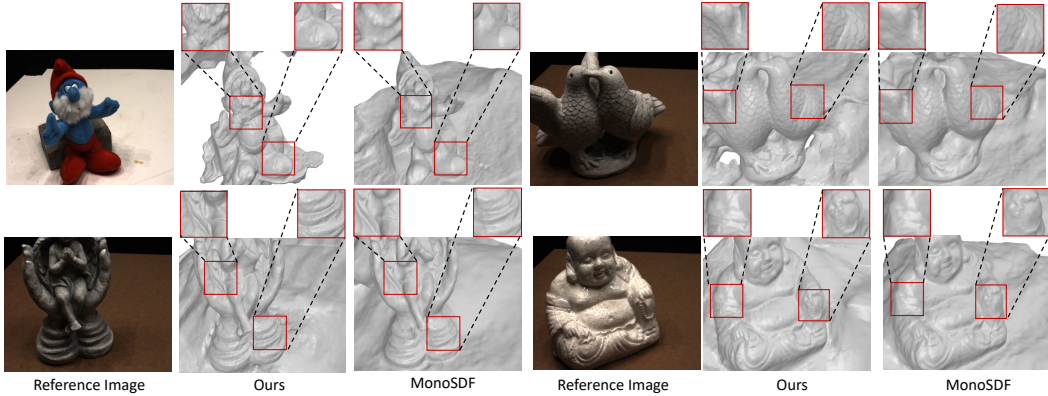


Figure 5: This figure compares the details on the reconstructed geometry, for sparse-view inputs on the DTU dataset, against the second-best competing method, MonoSDF (see Table 1). Our approach produces sharper details, which can be attributed to the surface guidance from the predicted templates.

encoded with 4 frequencies. We train the network for 300k iterations which takes roughly 8 hours on NVIDIA RTX 3090Ti GPU. After training, we extract the mesh using marching cubes [29] at a  $512^3$  resolution. See the Supplementary material for more details.

## 4 Results and Evaluation

**Datasets.** We use two commonly employed real-world object-scenes datasets, viz., DTU [18] and BlendedMVS dataset [58]. DTU dataset contains multi-view images (49-64) of different objects captured with a fixed camera and lighting parameters. For training sparse view reconstruction models, we use the same image IDs as in [36, 63, 61]. In addition to this, in order to show the generalization ability of our template prediction network we experiment with our method on the MobileBrick dataset [23], which consists of high-quality 3D models along with precise ground-truth annotations.

For the template learning stage, our training split consists of objects that do not overlap with the 15 test scans of the DTU dataset. We provide the list of scans used for training in the supplementary. We evaluate our method on standard 15 scans used for evaluation by [37, 60, 59, 51, 39]. The resolution of each image in the dataset is  $1200 \times 1600$ . Unlike MonoSDF [63] which resizes the images to  $384 \times 384$  resolution for training, we input the actual image resolution to our pipeline. The other dataset, BlendedMVS, consists of 113 scenes captured from multiple views, where each image is of resolution  $576 \times 768$ . Unlike DTU, BlendedMVS dataset has not been employed before in the sparse view setting, and as such, specific view IDs to train and test are not available. We therefore manually select 3 views that have little overlap.

**Baselines.** For sparse views, we compare against the classical MVS method, COLMAP [45], and recent volume rendering-based methods such as NeuS [51], VolSDF [59] and MonoSDF [63]. We exclude SparseNeuS [28] evaluation in disparate settings because of its inability to reconstruct 3D geometry when the input images have significantly less overlap. For dense views, we additionally compare against the recent grid-based method, Voxurf [54]. A mesh from COLMAP point cloud output is obtained using Screened Poisson Surface Reconstruction [21].

**Evaluation Metrics.** Following standard evaluation protocol, we use Chamfer Distance (CD) between the ground truth point cloud and predicted meshes to quantify the reconstruction quality. On the DTU dataset, following prior works [59, 51, 63], we report CD scores. On the BlendedMVS dataset, we simply show qualitative results as is commonly done in the literature. In addition to this, for evaluation on the MobileBrick dataset, we use F1 score computed using the ground-truth mesh.

### 4.1 Results on DTU

Figure 1 and Table 1 show qualitative and quantitative results, respectively, in the presence of sparse view inputs (three, to be specific) on the DTU dataset. We observe from Table 1 that our method outperforms all other competing methods, including MonoSDF [63], on nine of the fifteen scenes in the test set, and achieves the lowest mean CD score (the next best adds an additional 0.09 CD score).

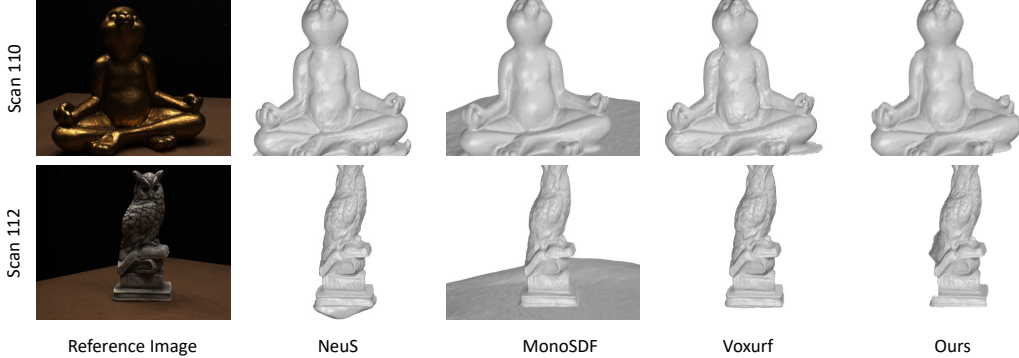


Figure 6: Dense view reconstruction results on the DTU dataset.

Table 1: Quantitative comparisons for *sparse and disparate* view 3D reconstruction on DTU dataset (Section 4.1). For Scan ID 110,  $\times$  indicates that COLMAP could not reconstruct any points.

		Chamfer Distance (CD) ( $\downarrow$ )														
Scan ID $\rightarrow$	24	37	40	55	63	65	69	83	97	105	106	110	114	118	122	Mean
COLMAP[44]	4.45	4.67	2.51	1.9	2.81	2.92	2.12	2.05	2.93	2.05	2.01	$\times$	1.1	2.72	1.64	2.56
VolSDF [59]	5.24	5.09	3.99	1.42	5.1	4.33	5.36	3.15	5.78	2.07	2.79	5.73	1.2	5.64	6.2	4.2
NeuS [51]	4.39	4.59	5.11	5.37	5.21	5.60	5.26	4.72	5.91	3.97	4.02	3.1	4.84	3.91	5.71	4.78
MonoSDF [63]	3.47	<b>3.61</b>	2.1	1.05	<b>2.37</b>	<b>1.38</b>	1.41	1.85	<b>1.74</b>	1.1	1.46	<b>2.28</b>	1.25	1.44	<b>1.45</b>	1.86
Ours	<b>3.37</b>	4.11	<b>1.46</b>	<b>0.75</b>	2.74	1.52	<b>1.13</b>	<b>1.63</b>	2.08	<b>0.98</b>	<b>0.87</b>	2.7	<b>0.47</b>	<b>1.24</b>	1.57	<b>1.77</b>

On the other six scans, our method is the second-best performing method behind MonoSDF. This is because our predicted templates are not always perfect for all objects, meaning, regions on the surface with no predicted templates potentially suffer from incomplete reconstructions. Other methods such as VolSDF [59] and NeuS [51] fail to even beat the classical MVS method, COLMAP [46], indicating that these methods either require dense view inputs[59] or require a significant amount of overlap on the input views [28] to faithfully reconstruct the surface. This emphasizes the effectiveness of our method on the disparate views case. Further, Figure 5 compares surface details on the reconstructed geometry against, MonoSDF [63], where it can be observed that our method produces sharper details, attributed mainly to the geometry guidance from learned template priors.

On dense view inputs (49-64), Figure 6 and Table 3 present qualitative and quantitative results, respectively, over the aforementioned techniques. We additionally compare against a recent method, Voxurf [54]. In this setting, all neural surface reconstruction

Table 2: Generalization of TPN on MobileBrick dataset.

		F1 Score ( $\uparrow$ )			
Object $\rightarrow$	Bridge	Camera	Colosseum	Castle	
Ours (pre-trained TPN)	0.565	0.61	0.219	0.175	
Ours (TPN re-training)	<b>0.658</b>	<b>0.67</b>	<b>0.22</b>	<b>0.187</b>	

methods outperform COLMAP, indicating that the presence of dense view inputs is necessary to tap into the learning ability of neural rendering techniques for improved geometry reconstruction. We observe that our method outperforms the rest on five scans, which is higher than any other method (Voxurf-three scans, NeuS-four, MonoSDF-two, and VolSDF-one). Overall, our method achieves the second-best mean CD score, closely trailing behind Voxurf (a difference of 0.03 CD score). This is expected as feature-grid-based approaches tend to reconstruct sharper details compared to MLP [63]. But otherwise, we beat all other existing works owing to our neural template regularization scheme. More qualitative results on dense view inputs are provided in the Supplementary material.

## 4.2 Results on BlendedMVS

We also run our pipeline on a more challenging, also real-world, BlendedMVS dataset [58]. We use the sparse input setting and show comparisons against the same set of prior works, i.e., NeuS[51] and MonoSDF [63]. Figure 7 shows qualitative results on 4 object-scenes with complex geometries. Clearly, our method obtains the best surface reconstruction. NeuS is not able to reconstruct the



Table 3: Quantitative comparisons for *dense-view* 3D reconstruction on DTU dataset (Section 4.1).

Scan ID →	Chamfer Distance (CD) (↓)															
	24	37	40	55	63	65	69	83	97	105	106	110	114	118	122	Mean
COLMAP[44]	0.81	2.05	0.73	1.22	1.79	1.58	1.02	3.05	1.4	2.05	1.0	1.32	0.49	0.78	1.17	1.36
NeuS[51]	1.0	1.37	0.93	0.43	1.1	<b>0.65</b>	<b>0.57</b>	1.48	<b>1.09</b>	0.83	<b>0.52</b>	1.2	0.35	0.49	0.54	0.84
VolSDF [59]	1.14	1.26	0.81	0.49	1.25	0.7	0.72	<b>1.29</b>	1.18	0.7	0.66	1.08	0.42	0.61	0.55	0.86
MonoSDF [63]	0.83	1.61	0.65	0.47	<b>0.92</b>	0.87	0.87	1.3	1.25	<b>0.68</b>	0.65	0.96	0.41	0.62	0.58	0.84
Voxurf [54]	0.91	<b>0.73</b>	<b>0.45</b>	<b>0.34</b>	0.99	0.66	0.83	1.36	1.31	0.78	0.53	1.12	0.37	0.53	0.51	<b>0.76</b>
Ours	<b>0.78</b>	1.29	0.68	0.42	0.96	0.70	0.68	1.43	1.30	0.827	0.62	<b>0.94</b>	<b>0.34</b>	<b>0.49</b>	<b>0.49</b>	0.79

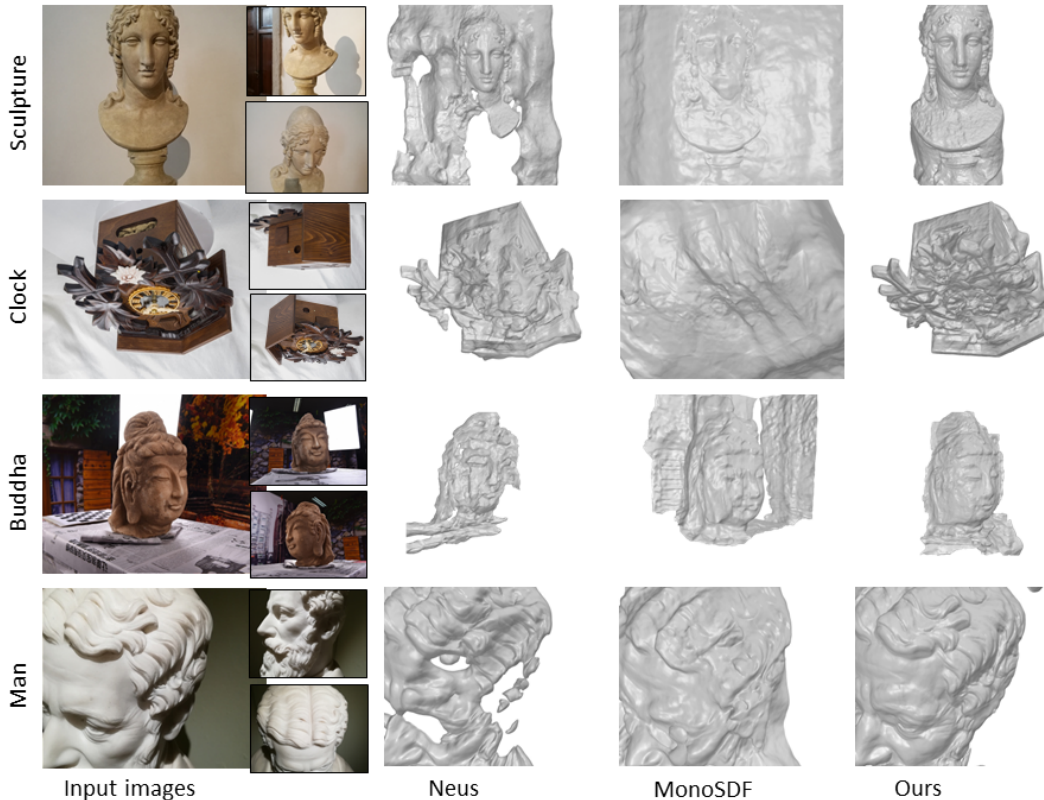


Figure 7: Qualitative reconstruction results for three disparate view inputs on the challenging BlendedMVS dataset [58]. See Section 4.2 and the Supplementary for a more details explanation.

geometry faithfully for any of the objects due to disparate view inputs. MonoSDF, on the other hand, despite using ground truth depth and normal cues, fails to reconstruct accurate geometry, especially for Clock and Sculpture objects. In contrast to this, our method can accurately reconstruct the geometric details owing to template guidance coming from Stage 1.

### 4.3 Generalization on MobileBrick Dataset

We test the generalization ability of our template prediction network (TPN) on a new dataset, MobileBrick [23], by comparing the reconstruction results when the neural templates were learned by a pre-trained TPN (on DTU) vs. when they were trained on MobileBrick. Note that overall, the models from these two datasets are quite different in terms of geometry and structure. The results in Table 2 and qualitative results in Figure 8a (a) show that the reconstruction qualities under the two scenarios are comparable, attesting to the generalizability of our TPN. As mentioned before, the metric used in this evaluation is F1 score as reported by MobileBrick dataset.

### 4.4 Ablation Studies

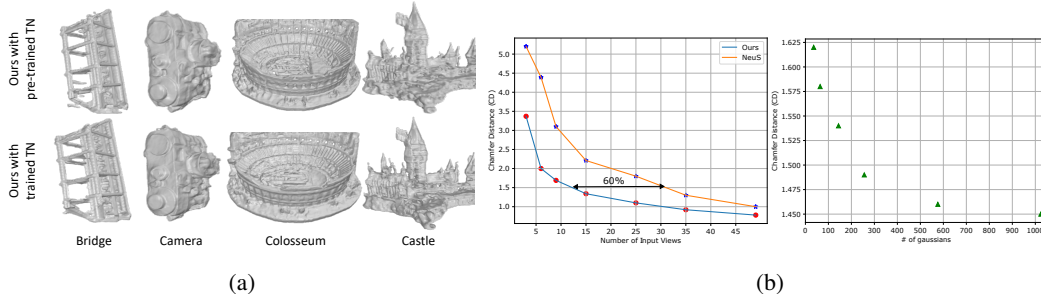


Figure 8: (a) Generalization of TPN on MobileBrick Dataset. (b) Effect on chamfer distance with # of Views (left) and Gaussians (right).

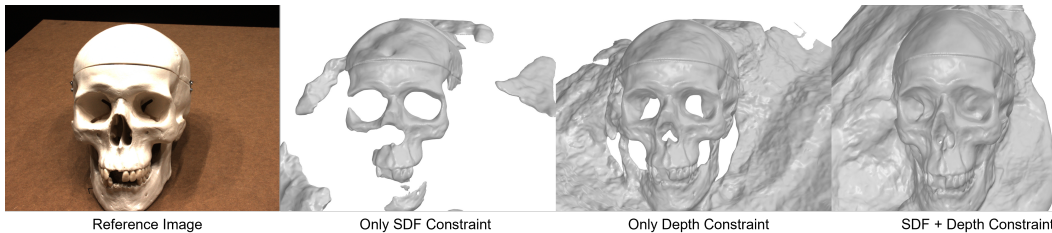


Figure 9: Effect of different optimization constraints (Figure 2, Section 3.2) employed in our pipeline.

In Figure 9, we demonstrate the need for employing different loss functions as described in Section 3.2 and depicted on the right side of Figure 2 and Table 4. We observe how the reconstructed geometry changes when  $\mathcal{L}_{sdf}$  and  $\mathcal{L}_{depth}$  are separately employed. Evidently, only SDF constraints cannot reconstruct surfaces due to the coarse supervision from template centers. On the other hand, depth regularization significantly improves the reconstruction but holes still exist. Our full pipeline includes both the above constraints, resulting in improved reconstruction, as can be seen in the last column of Figure 9 and Table 4. We also study reconstruction quality as a function of the number of input views. Figure 8b depicts the behavior of two such methods i.e. NeuS and Ours, up to fifty views. Our method achieves the same Chamfer Distance (CD) score for twelve views as NeuS achieves for around thirty. This demonstrates the efficacy of our method to “catch” surface geometry even when sufficient view inputs are not present. In addition to this, we measure the effect on reconstruction quality by varying the number of Gaussians. As it can be seen in Figure 8b the surface reconstruction quality significantly improves as we increase the number of Gaussians. The reconstruction quality saturates after 576 Gaussians and hence we use 576 Gaussians throughout our experiments.

Table 4: Impact of each constraint.

	CD ( $\downarrow$ )
Only SDF Constraint	2.70
Only Depth Constraint	1.96
<b>SDF + Depth Constraint</b>	<b>1.52</b>

## 5 Discussions, Limitations and Future Work

We present DiViNet for sparse multi-view 3D reconstruction. Our core idea is a simple two-stage framework with neural Gaussian templates learned across different scenes serving as surface priors to regularize the volume-rendering-based reconstruction. Experiments demonstrate quality reconstructions by DiViNet in both dense and sparse+disparate view settings, with clearly superior performance over state-of-the-art in the latter.

One current limitation of our method is its reconstruction speed. While comparable to NeuS [51], VolSDF [59], and MonoSDF [63], it is still slow due to the two-stage approach, especially when generalizing to a large number of real-world scenes. In addition to addressing these issues, e.g., dynamic templates, we would also like to replace the MLPs in DiViNet with more efficient grid-based techniques, e.g., instant NGP [35], and explore more general primitives such as convexes and super-quadratics in place of Gaussians.

## 6 Acknowledgements

We thank the anonymous reviewers for their valuable comments and Sherwin Bahmani and Yizhi Wang for discussions during rebuttal and helping with the renderings in the paper. This research is supported in part by a Discovery Grant from NSERC (No. 611370).

## References

- [1] M. Agrawal and L. S. Davis. A probabilistic framework for surface reconstruction from multiple images. In *Proceedings of the 2001 IEEE Computer Society Conference on Computer Vision and Pattern Recognition. CVPR 2001*, volume 2, pages II–II. IEEE, 2001.
- [2] M. Atzmon and Y. Lipman. Sal: Sign agnostic learning of shapes from raw data. In *Proceedings of the IEEE/CVF Conference on Computer Vision and Pattern Recognition*, pages 2565–2574, 2020.
- [3] M. Bleyer, C. Rhemann, and C. Rother. Patchmatch stereo-stereo matching with slanted support windows. In *Bmvc*, volume 11, pages 1–11, 2011.
- [4] A. Broadhurst, T. W. Drummond, and R. Cipolla. A probabilistic framework for space carving. In *Proceedings eighth IEEE international conference on computer vision. ICCV 2001*, volume 1, pages 388–393. IEEE, 2001.
- [5] A. Chen, Z. Xu, F. Zhao, X. Zhang, F. Xiang, J. Yu, and H. Su. MVSNeRF: Fast generalizable radiance field reconstruction from multi-view stereo. In *Proceedings of the IEEE/CVF International Conference on Computer Vision*, pages 14124–14133, 2021.
- [6] F. Darmon, B. Bascle, J.-C. Devaux, P. Monasse, and M. Aubry. Improving neural implicit surfaces geometry with patch warping. In *Proceedings of the IEEE/CVF Conference on Computer Vision and Pattern Recognition*, pages 6260–6269, 2022.
- [7] J. S. De Bonet and P. Viola. Poxels: Probabilistic voxelized volume reconstruction. In *Proceedings of International Conference on Computer Vision (ICCV)*, volume 2, page 3, 1999.
- [8] K. Deng, A. Liu, J.-Y. Zhu, and D. Ramanan. Depth-supervised NeRF: Fewer views and faster training for free. In *Proceedings of the IEEE/CVF Conference on Computer Vision and Pattern Recognition*, pages 12882–12891, 2022.
- [9] Q. Fu, Q. Xu, Y. S. Ong, and W. Tao. Geo-neus: Geometry-consistent neural implicit surfaces learning for multi-view reconstruction. *Advances in Neural Information Processing Systems*, 35:3403–3416, 2022.
- [10] Y. Furukawa, C. Hernández, et al. Multi-view stereo: A tutorial. *Foundations and Trends® in Computer Graphics and Vision*, 9(1-2):1–148, 2015.
- [11] K. Genova, F. Cole, A. Sud, A. Sarna, and T. Funkhouser. Local deep implicit functions for 3d shape. In *Proceedings of the IEEE/CVF Conference on Computer Vision and Pattern Recognition*, pages 4857–4866, 2020.
- [12] K. Genova, F. Cole, D. Vlasic, A. Sarna, W. T. Freeman, and T. Funkhouser. Learning shape templates with structured implicit functions. In *Proceedings of the IEEE/CVF International Conference on Computer Vision*, pages 7154–7164, 2019.
- [13] M. Goesele, B. Curless, and S. M. Seitz. Multi-view stereo revisited. In *2006 IEEE Computer Society Conference on Computer Vision and Pattern Recognition (CVPR’06)*, volume 2, pages 2402–2409. IEEE, 2006.
- [14] A. Gropp, L. Yariv, N. Haim, M. Atzmon, and Y. Lipman. Implicit geometric regularization for learning shapes. *arXiv preprint arXiv:2002.10099*, 2020.
- [15] X. Gu, Z. Fan, S. Zhu, Z. Dai, F. Tan, and P. Tan. Cascade cost volume for high-resolution multi-view stereo and stereo matching. In *Proceedings of the IEEE/CVF conference on computer vision and pattern recognition*, pages 2495–2504, 2020.

- [16] J. Huang, Z. Gojcic, M. Atzmon, O. Litany, S. Fidler, and F. Williams. Neural kernel surface reconstruction. In *Proceedings of the IEEE/CVF Conference on Computer Vision and Pattern Recognition*, pages 4369–4379, 2023.
- [17] P.-H. Huang, K. Matzen, J. Kopf, N. Ahuja, and J.-B. Huang. Deepmvs: Learning multi-view stereopsis. In *Proceedings of the IEEE Conference on Computer Vision and Pattern Recognition*, pages 2821–2830, 2018.
- [18] R. Jensen, A. Dahl, G. Vogiatzis, E. Tola, and H. Aanæs. Large scale multi-view stereopsis evaluation. In *2014 IEEE Conference on Computer Vision and Pattern Recognition*, pages 406–413. IEEE, 2014.
- [19] Y. Jiang, D. Ji, Z. Han, and M. Zwicker. Sdfdiff: Differentiable rendering of signed distance fields for 3d shape optimization. In *Proceedings of the IEEE/CVF Conference on Computer Vision and Pattern Recognition*, pages 1251–1261, 2020.
- [20] H. Kato, D. Beker, M. Morariu, T. Ando, T. Matsuoka, W. Kehl, and A. Gaidon. Differentiable rendering: A survey. *CoRR*, abs/2006.12057, 2020.
- [21] M. Kazhdan and H. Hoppe. Screened poisson surface reconstruction. *ACM Transactions on Graphics (ToG)*, 32(3):1–13, 2013.
- [22] D. P. Kingma, J. A. Ba, and J. Adam. A method for stochastic optimization. arxiv 2014. *arXiv preprint arXiv:1412.6980*, 106, 2020.
- [23] K. Li, J.-W. Bian, R. Castle, P. H. Torr, and V. A. Prisacariu. Mobilebrick: Building lego for 3d reconstruction on mobile devices. In *Proceedings of the IEEE/CVF Conference on Computer Vision and Pattern Recognition*, pages 4892–4901, 2023.
- [24] Z. Li, T. Müller, A. Evans, R. H. Taylor, M. Unberath, M.-Y. Liu, and C.-H. Lin. Neuralangelo: High-fidelity neural surface reconstruction. In *Proceedings of the IEEE/CVF Conference on Computer Vision and Pattern Recognition*, pages 8456–8465, 2023.
- [25] L. Liu, J. Gu, K. Zaw Lin, T.-S. Chua, and C. Theobalt. Neural sparse voxel fields. *Advances in Neural Information Processing Systems*, 33:15651–15663, 2020.
- [26] S. Liu, Y. Zhang, S. Peng, B. Shi, M. Pollefeys, and Z. Cui. Dist: Rendering deep implicit signed distance function with differentiable sphere tracing. In *Proceedings of the IEEE/CVF Conference on Computer Vision and Pattern Recognition*, pages 2019–2028, 2020.
- [27] S. Lombardi, T. Simon, J. Saragih, G. Schwartz, A. Lehrmann, and Y. Sheikh. Neural volumes: Learning dynamic renderable volumes from images. *arXiv preprint arXiv:1906.07751*, 2019.
- [28] X. Long, C. Lin, P. Wang, T. Komura, and W. Wang. SparseNeuS: Fast generalizable neural surface reconstruction from sparse views. In *Computer Vision—ECCV 2022: 17th European Conference, Tel Aviv, Israel, October 23–27, 2022, Proceedings, Part XXXII*, pages 210–227. Springer, 2022.
- [29] W. E. Lorensen and H. E. Cline. Marching cubes: A high resolution 3d surface construction algorithm. *ACM siggraph computer graphics*, 21(4):163–169, 1987.
- [30] W. Luo, A. G. Schwing, and R. Urtasun. Efficient deep learning for stereo matching. In *Proceedings of the IEEE conference on computer vision and pattern recognition*, pages 5695–5703, 2016.
- [31] N. Max. Optical models for direct volume rendering. *IEEE Transactions on Visualization and Computer Graphics*, 1(2):99–108, 1995.
- [32] L. Mescheder, M. Oechsle, M. Niemeyer, S. Nowozin, and A. Geiger. Occupancy networks: Learning 3d reconstruction in function space. In *Proceedings of the IEEE/CVF conference on computer vision and pattern recognition*, pages 4460–4470, 2019.
- [33] M. Michalkiewicz, J. K. Pontes, D. Jack, M. Baktashmotlagh, and A. Eriksson. Deep level sets: Implicit surface representations for 3d shape inference. *arXiv preprint arXiv:1901.06802*, 2019.

- [34] B. Mildenhall, P. P. Srinivasan, M. Tancik, J. T. Barron, R. Ramamoorthi, and R. Ng. NeRF: Representing scenes as neural radiance fields for view synthesis. *Communications of the ACM*, 65(1):99–106, 2021.
- [35] T. Müller, A. Evans, C. Schied, and A. Keller. Instant neural graphics primitives with a multiresolution hash encoding. *ACM Transactions on Graphics (ToG)*, 41(4):1–15, 2022.
- [36] M. Niemeyer, J. T. Barron, B. Mildenhall, M. S. Sajjadi, A. Geiger, and N. Radwan. RegNeRF: Regularizing neural radiance fields for view synthesis from sparse inputs. In *Proceedings of the IEEE/CVF Conference on Computer Vision and Pattern Recognition*, pages 5480–5490, 2022.
- [37] M. Niemeyer, L. Mescheder, M. Oechsle, and A. Geiger. Differentiable volumetric rendering: Learning implicit 3d representations without 3d supervision. In *Proceedings of the IEEE/CVF Conference on Computer Vision and Pattern Recognition*, pages 3504–3515, 2020.
- [38] C. Niu, M. Li, K. Xu, and H. Zhang. RIM-Net: Recursive implicit fields for unsupervised learning of hierarchical shape structures. In *Proceedings of the IEEE/CVF Conference on Computer Vision and Pattern Recognition*, pages 11779–11788, 2022.
- [39] M. Oechsle, S. Peng, and A. Geiger. Unisurf: Unifying neural implicit surfaces and radiance fields for multi-view reconstruction. In *Proceedings of the IEEE/CVF International Conference on Computer Vision*, pages 5589–5599, 2021.
- [40] J. J. Park, P. Florence, J. Straub, R. Newcombe, and S. Lovegrove. DeepSDF: Learning continuous signed distance functions for shape representation. In *Proceedings of the IEEE/CVF conference on computer vision and pattern recognition*, pages 165–174, 2019.
- [41] A. Paszke, S. Gross, S. Chintala, G. Chanan, E. Yang, Z. DeVito, Z. Lin, A. Desmaison, L. Antiga, and A. Lerer. Automatic differentiation in pytorch. 2017.
- [42] G. Riegler, A. O. Ulusoy, H. Bischof, and A. Geiger. Octnetfusion: Learning depth fusion from data. In *2017 International Conference on 3D Vision (3DV)*, pages 57–66. IEEE, 2017.
- [43] S. Saito, Z. Huang, R. Natsume, S. Morishima, A. Kanazawa, and H. Li. Pifu: Pixel-aligned implicit function for high-resolution clothed human digitization. In *Proceedings of the IEEE/CVF international conference on computer vision*, pages 2304–2314, 2019.
- [44] J. L. Schönberger and J.-M. Frahm. Structure-from-motion revisited. In *Conference on Computer Vision and Pattern Recognition (CVPR)*, 2016.
- [45] J. L. Schönberger, E. Zheng, J.-M. Frahm, and M. Pollefeys. Pixelwise view selection for unstructured multi-view stereo. In *Computer Vision—ECCV 2016: 14th European Conference, Amsterdam, The Netherlands, October 11–14, 2016, Proceedings, Part III 14*, pages 501–518. Springer, 2016.
- [46] J. L. Schönberger, E. Zheng, M. Pollefeys, and J.-M. Frahm. Pixelwise view selection for unstructured multi-view stereo. In *European Conference on Computer Vision (ECCV)*, 2016.
- [47] S. M. Seitz, B. Curless, J. Diebel, D. Scharstein, and R. Szeliski. A comparison and evaluation of multi-view stereo reconstruction algorithms. In *2006 IEEE computer society conference on computer vision and pattern recognition (CVPR'06)*, volume 1, pages 519–528. IEEE, 2006.
- [48] S. M. Seitz and C. R. Dyer. Photorealistic scene reconstruction by voxel coloring. *International journal of computer vision*, 35:151–173, 1999.
- [49] V. Sitzmann, M. Zollhöfer, and G. Wetzstein. Scene representation networks: Continuous 3d-structure-aware neural scene representations. *Advances in Neural Information Processing Systems*, 32, 2019.
- [50] B. Ummenhofer, H. Zhou, J. Uhrig, N. Mayer, E. Ilg, A. Dosovitskiy, and T. Brox. Demon: Depth and motion network for learning monocular stereo. In *Proceedings of the IEEE conference on computer vision and pattern recognition*, pages 5038–5047, 2017.

- [51] P. Wang, L. Liu, Y. Liu, C. Theobalt, T. Komura, and W. Wang. Neus: Learning neural implicit surfaces by volume rendering for multi-view reconstruction. *arXiv preprint arXiv:2106.10689*, 2021.
- [52] Q. Wang, Z. Wang, K. Genova, P. P. Srinivasan, H. Zhou, J. T. Barron, R. Martin-Brualla, N. Snavely, and T. Funkhouser. Ibrnet: Learning multi-view image-based rendering. In *Proceedings of the IEEE/CVF Conference on Computer Vision and Pattern Recognition*, pages 4690–4699, 2021.
- [53] Y. Wei, S. Liu, J. Zhou, and J. Lu. Depth-guided optimization of neural radiance fields for indoor multi-view stereo. *IEEE Transactions on Pattern Analysis and Machine Intelligence*, 2023.
- [54] T. Wu, J. Wang, X. Pan, X. Xu, C. Theobalt, Z. Liu, and D. Lin. Voxurf: Voxel-based efficient and accurate neural surface reconstruction. *arXiv preprint arXiv:2208.12697*, 2022.
- [55] Y. Xie, T. Takikawa, S. Saito, O. Litany, S. Yan, N. Khan, F. Tombari, J. Tompkin, V. Sitzmann, and S. Sridhar. Neural fields in visual computing and beyond. *Computer Graphics Forum*, 2022.
- [56] Q. Xu, Z. Xu, J. Philip, S. Bi, Z. Shu, K. Sunkavalli, and U. Neumann. Point-nerf: Point-based neural radiance fields. In *Proceedings of the IEEE/CVF Conference on Computer Vision and Pattern Recognition*, pages 5438–5448, 2022.
- [57] Y. Yao, Z. Luo, S. Li, T. Fang, and L. Quan. Mvsnet: Depth inference for unstructured multi-view stereo. In *Proceedings of the European conference on computer vision (ECCV)*, pages 767–783, 2018.
- [58] Y. Yao, Z. Luo, S. Li, J. Zhang, Y. Ren, L. Zhou, T. Fang, and L. Quan. Blendedmvs: A large-scale dataset for generalized multi-view stereo networks. In *Proceedings of the IEEE/CVF Conference on Computer Vision and Pattern Recognition*, pages 1790–1799, 2020.
- [59] L. Yariv, J. Gu, Y. Kasten, and Y. Lipman. Volume rendering of neural implicit surfaces. *Advances in Neural Information Processing Systems*, 34:4805–4815, 2021.
- [60] L. Yariv, Y. Kasten, D. Moran, M. Galun, M. Atzmon, B. Ronen, and Y. Lipman. Multiview neural surface reconstruction by disentangling geometry and appearance. *Advances in Neural Information Processing Systems*, 33:2492–2502, 2020.
- [61] A. Yu, V. Ye, M. Tancik, and A. Kanazawa. PixelNeRF: Neural radiance fields from one or few images. In *Proceedings of the IEEE/CVF Conference on Computer Vision and Pattern Recognition*, pages 4578–4587, 2021.
- [62] Z. Yu and S. Gao. Fast-mvsnet: Sparse-to-dense multi-view stereo with learned propagation and gauss-newton refinement. In *Proceedings of the IEEE/CVF Conference on Computer Vision and Pattern Recognition*, pages 1949–1958, 2020.
- [63] Z. Yu, S. Peng, M. Niemeyer, T. Sattler, and A. Geiger. Monosdf: Exploring monocular geometric cues for neural implicit surface reconstruction. *arXiv preprint arXiv:2206.00665*, 2022.
- [64] S. Zagoruyko and N. Komodakis. Learning to compare image patches via convolutional neural networks. In *Proceedings of the IEEE conference on computer vision and pattern recognition*, pages 4353–4361, 2015.
- [65] J. Zhang, Y. Yao, S. Li, T. Fang, D. McKinnon, Y. Tsin, and L. Quan. Critical regularizations for neural surface reconstruction in the wild. In *Proceedings of the IEEE/CVF Conference on Computer Vision and Pattern Recognition*, pages 6270–6279, 2022.
- [66] K. Zhang, G. Riegler, N. Snavely, and V. Koltun. Nerf++: Analyzing and improving neural radiance fields. *arXiv preprint arXiv:2010.07492*, 2020.
- [67] X. Zhang, S. Bi, K. Sunkavalli, H. Su, and Z. Xu. NeRFusion: Fusing radiance fields for large-scale scene reconstruction. In *Proceedings of the IEEE/CVF Conference on Computer Vision and Pattern Recognition*, pages 5449–5458, 2022.

# - Supplementary -

## A Architecture & Implementation Details

We present a novel approach for a volume rendering-based surface reconstruction, which takes as few as 3 images as input. Below are the details of each step.

### A.1 Template Prediction network architecture.

Inspired by the generalization approaches of neural radiance field [5, 61, 56], we take a similar approach for our template learning step. Our network  $\mathcal{T}_{\theta_0}$  is composed of an encoder ( $\mathcal{E}$ ) and 2 decoders i.e. geometry decoder ( $\mathcal{D}_{geo}$ ), and voxel feature-grid decoder ( $\mathcal{D}_{vox}$ ).

**Encoder ( $\mathcal{E}$ ).** The encoder ( $\mathcal{E}$ ) is adapted from [57]. There are a total of 5 convolutional layers in the encoder, which downsamples the image by a factor of 32. Hence, with  $N$  images as input at a resolution of  $512 \times 512 \times 3$ , we obtain a feature of size  $N \times C \times 16 \times 16$ , post the forward pass. Here,  $C$  is the number of feature channels obtained at the output ( $C = 64$ ). Using these features obtained from the encoder, we sample per template feature using bilinear interpolation. We concatenate all the interpolated template features  $\{f_i\}_{i=1}^{\mathcal{N}_t}$  into a tensor of size  $\mathcal{N}_t \times N \times C$ .

We aggregate the multi-view features of each template, obtained from images using the feature-pooling strategy proposed in [52]. This allows us to input any number of images as input. Specifically, we first compute the element-wise mean,  $\mu$ , and variance,  $v$  for each feature obtained from the encoder  $\mathcal{E}$ . We then concatenate each feature with the computed,  $\mu$  and  $v$  and feed it through the shared MLP followed by a softmax to predict the weight  $\{w_i\}_{i=1}^{\mathcal{N}_t}$  for each multi-view feature. We then blend all the features from all views using the predicted blend weights  $\{w_i\}_{i=1}^{\mathcal{N}_t}$ . Post this step, the template features  $\{f_i\}_{i=1}^{\mathcal{N}_t}$  gets transformed into a tensor of size  $\mathcal{N}_t \times C$ .

**Decoders ( $\mathcal{D}_{geo}$  and  $\mathcal{D}_{vox}$ ).**  $\mathcal{D}_{geo}$  is used to predict the template parameters, whereas  $\mathcal{D}_{vox}$  predicts voxel-grid features for each template. We decode these features channel-wise into a feature of dimension  $C \cdot \mathcal{M} \times \sqrt{\mathcal{N}_t} \cdot \mathcal{M} \times \sqrt{\mathcal{N}_t} \cdot \mathcal{M}$ . We then reshape these features to a volumetric feature grid of dimension  $C \times \mathcal{M} \times \sqrt{\mathcal{N}_t} \cdot \mathcal{M} \times \sqrt{\mathcal{N}_t} \cdot \mathcal{M}$ . Here,  $C = 8$ ,  $\mathcal{M} = 16$ . The architectures are illustrated in Table 5 6.

### A.2 Training Details.

To learn generalizable templates, we train our template prediction network end-to-end across different objects from DTU [18] and BlendedMVS datasets [58]. For the DTU dataset, we use 15 scenes for testing, which are the same scenes used by [60]. The remaining non-overlapping 75 scenes are used for training our template prediction network. This split is the same split that is used by [28].

The BlendedMVS [58] dataset, contains  $> 100$  scenes, captured in both indoor and outdoor settings. This includes many scenes with complex architecture and backgrounds. We exclude these complex large-scale scenes in our template training. Out of all the objects, we select 35 objects for training the template prediction network and, following [59, 51, 28] we select 7 other non-overlapping objects for the test split which we use to train our surface reconstruction model.

### A.3 Sparse Reconstruction using COLMAP.

Before the template training stage, we reconstruct a sparse point cloud for all the objects in our train split using COLMAP [46]. This point cloud acts as a "free" supervision [8, 56] for the optimization of our template prediction network. To reconstruct the point cloud, we run COLMAP in triangulation mode, with all the provided images and ground truth camera poses of objects in the train split. We use these sparse reconstructed point clouds to optimize our template prediction network.

Table 5: The architecture of the two decoders,  $\mathcal{D}_{geo}$  and  $\mathcal{D}_{vox}$ . Each template feature is,  $f_i$ . A hidden feature of each template is,  $h_i$ .  $[C_t, R_t, S_t]$  is the set of centers, radii, and scales of all the templates. L=Linear, R=ReLU, TCN=Transposed Convolution. The volumetric feature grid of each template is of size  $16 \times 16 \times 16$ . We use a total of  $576(24^2)$  templates.

Decoder	Layer	Channels	Input	Output
$\mathcal{D}_{geo}$	$LR_{[0-3]}$	64 / 64	$f_i$	$h_i$
	$L_{ctr}$	64 / 3	$h_i$	$C_t$
	$L_{rad}$	64 / 3	$h_i$	$R_t$
	$L_{scale}$	64 / 1	$h_i$	$S_t$
$\mathcal{D}_{vox}$	$TCN_0$	64	$24 \cdot 1 \times 24 \cdot 1 \times 64$	$24 \cdot 2 \times 24 \cdot 2 \times 64$
	$TCN_1$	32	$24 \cdot 2 \times 24 \cdot 2 \times 64$	$24 \cdot 4 \times 24 \cdot 4 \times 32$
	$TCN_2$	64	$24 \cdot 4 \times 24 \cdot 4 \times 32$	$24 \cdot 8 \times 24 \cdot 8 \times 64$
	$TCN_3$	$16 \times 8$	$24 \cdot 8 \times 24 \cdot 8 \times 64$	$24 \cdot 16 \times 24 \cdot 16 \times 16 \cdot 8$

Table 6: Architecture of the MLP used to regress colors,  $\mathbf{c}$  at point locations  $\mathbf{p}$  in 3D space.  $f_{vox}(\mathbf{p})$  is the per-point feature obtained from tri-linear interpolation.

Layer	Channels	Input	Output
Reshape	-	$24 \cdot 16 \times 24 \cdot 16 \times 16 \cdot 8$	$24 \cdot 16 \times 24 \cdot 16 \times 16 \cdot 8$
$LR_0$	$3 + 8 / 256$	$\mathbf{p}, f_{vox}(\mathbf{p})$	hidden feature
$LR_1$	$256 / 3$	hidden feature	$\mathbf{c}$

## B Additional Results

### B.1 BlendedMVS Dataset

We show additional results on the BlendedMVS dataset for 3 new objects. As can be in Figure 11 our reconstruction quality significantly outperforms NeuS [51] and MonoSDF [63]. This shows that our method is capable to do surface reconstruction from disparate views even in complex settings. In contrast to this, MonoSDF with MLP fails to reconstruct the geometry faithfully. Whereas, NeuS [51] without any regularization has holes in the reconstruction. We show the images used to train the surface reconstruction model alongside the reconstruction results.

### B.2 DTU Sparse Views

Figure 10 shows additional qualitative comparison results on DTU scans with 3 views as input. We compare our method with NeuS [51] and MonoSDF [63]. As can be seen, our method achieves superior reconstruction quality compared to both NeuS and MonoSDF. We are able to achieve this, without using any explicit ground truth information. In contrast to this, MonoSDF uses pixel-accurate depth and normal map predictions in order to regularize the surface reconstruction process in sparse view settings.

### B.3 DTU Dense Views

Figure 12 shows additional qualitative comparison results on DTU scans with dense views as input. We compare our method against [51, 63, 54] for dense views. As it can be seen our method can achieve equally good reconstruction quality when dense views are provided as input.

### B.4 Additional Comparisons on MobileBrick Dataset

In addition, we also compare our method against GeoNeus [9] which uses a sparse reconstructed point cloud from COLMAP [45] and photometric consistency to regularize the surface reconstruction from dense views. In the case of scenes that are captured in the wild, COLMAP reconstruction is often noisy. Using this point cloud for regularization can negatively affect the reconstruction as observed in [24]. In contrast to this, DiViNet uses template priors which are trained across data. Such



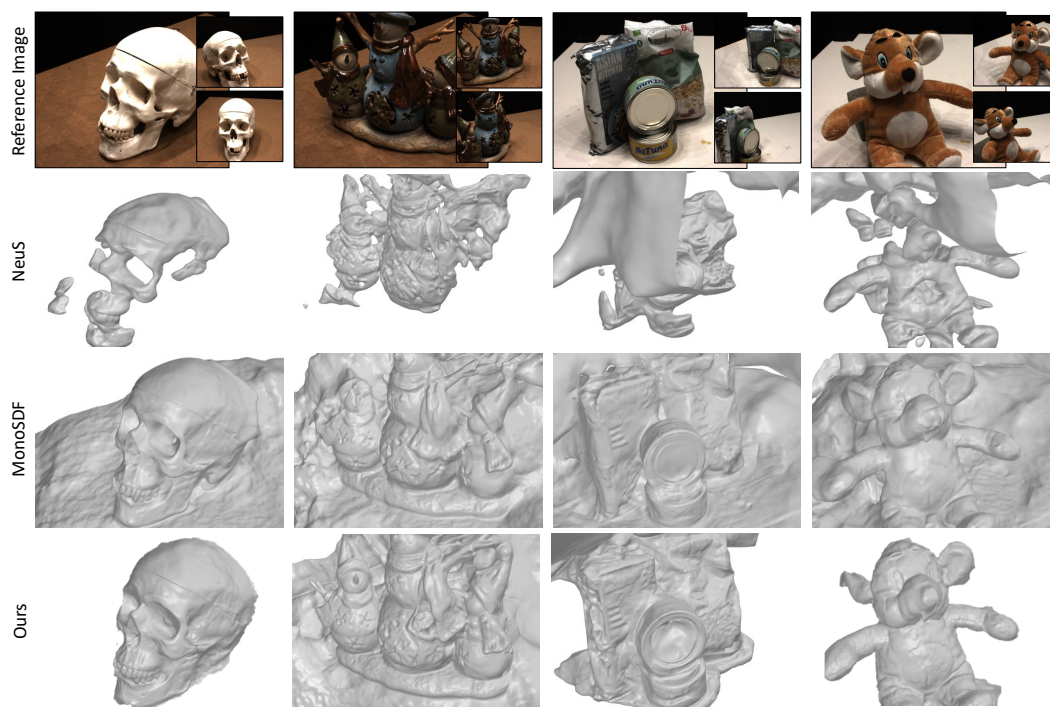


Figure 10: Results on DTU dataset with 3 views.

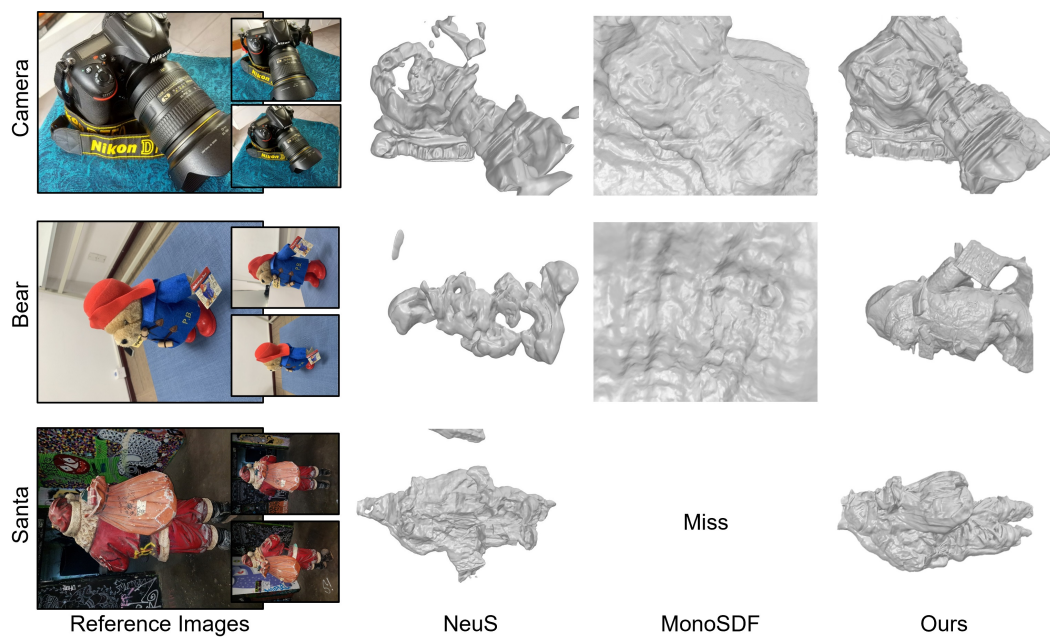


Figure 11: Results on BMVS dataset with 3 views. "Miss" represents the absence of reconstruction because of the "Out of Memory" issue.

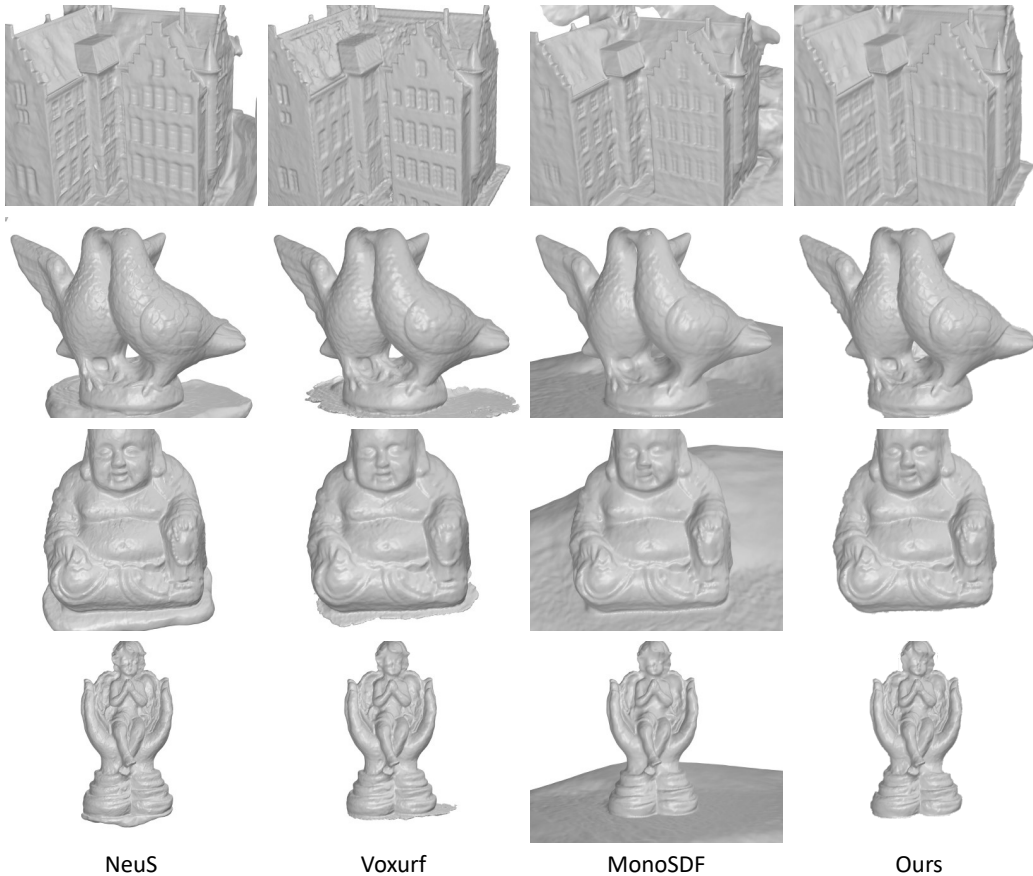


Figure 12: Results on DTU dataset with dense views.

Table 7: Quantitative Comparison on Mobilebrick dataset with GeoNeuS.

Object $\rightarrow$	F1 Score ( $\uparrow$ )			
	Bridge	Camera	Colosseum	Castle
GeoNeuS [9]	0.74	0.73	0.36	0.457
Ours	<b>0.915</b>	<b>0.846</b>	<b>0.415</b>	<b>0.572</b>

data-driven priors have been shown to be immune to outliers and noise [16]. We validate this by comparing our results with GeoNeuS on dense views on the MobileBrick dataset [23]. The qualitative results are shown in Figure 13 and quantitative results are shown in Table 7.

### B.5 Novel View Synthesis

Figure 14, 15, 16 shows the novel view synthesis results of different objects from the DTU dataset. As can be seen from the figures, our method achieves better view synthesis quality compared to MonoSDF on unseen views. Table 8 shows the quantitative results.

Table 8: Quantitative results of Novel View Synthesis.

	PSNR ( $\uparrow$ )	SSIM ( $\uparrow$ )	LPIPS ( $\downarrow$ )
MonoSDF [63]	23.64	—	—
Ours	<b>24.34</b>	<b>0.7208</b>	<b>0.264</b>

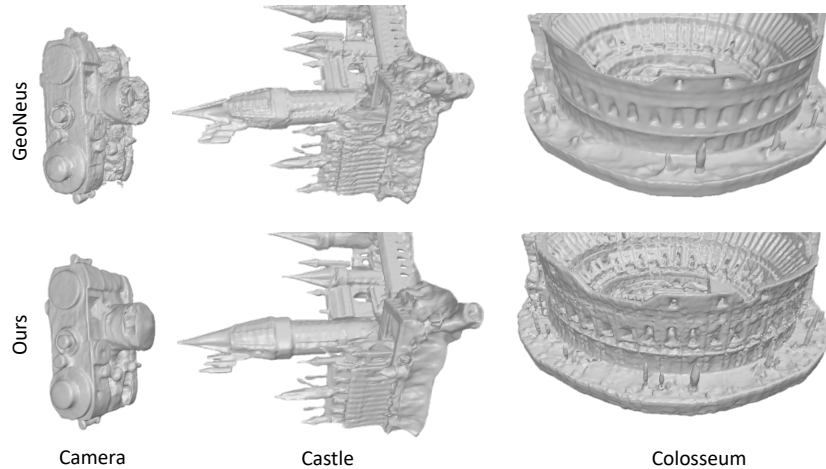


Figure 13: Qualitative Comparison with GeoNeus.

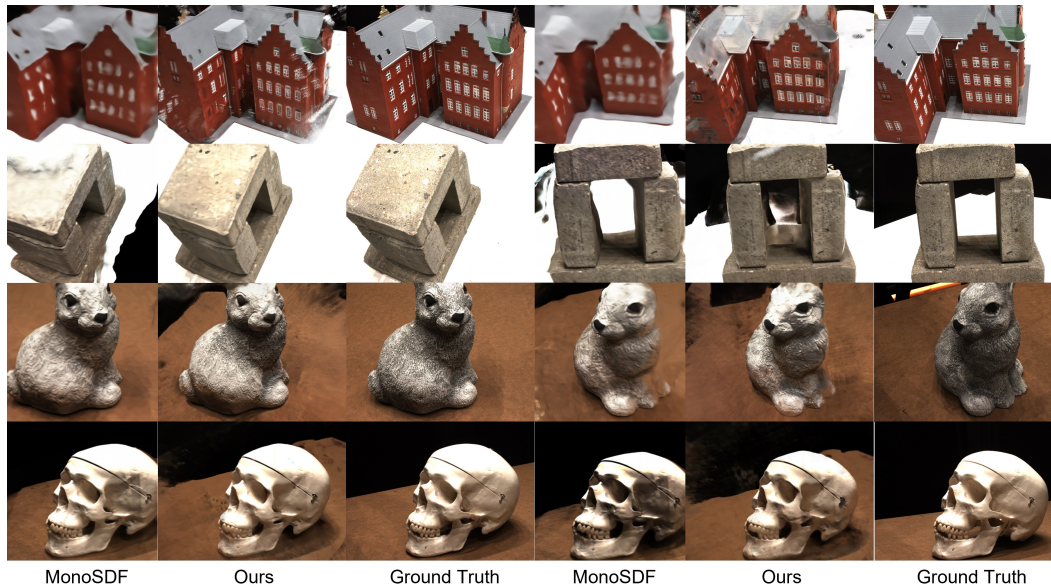


Figure 14: Novel View Synthesis Results on DTU dataset trained using 3 views.

## B.6 DTU Template Predictions

Figure 17 shows our template predictions on the DTU objects on the test split. During the inference of our templates on the test split, it is possible that the templates contain outliers i.e. those whose centers are not near the surface and have skewed radii. Hence, we do an outlier removal step, where we remove the templates whose centers and radii are 2 standard deviation away from the mean center and radii of templates respectively. In Figure 17 we show results after the outlier removal step.

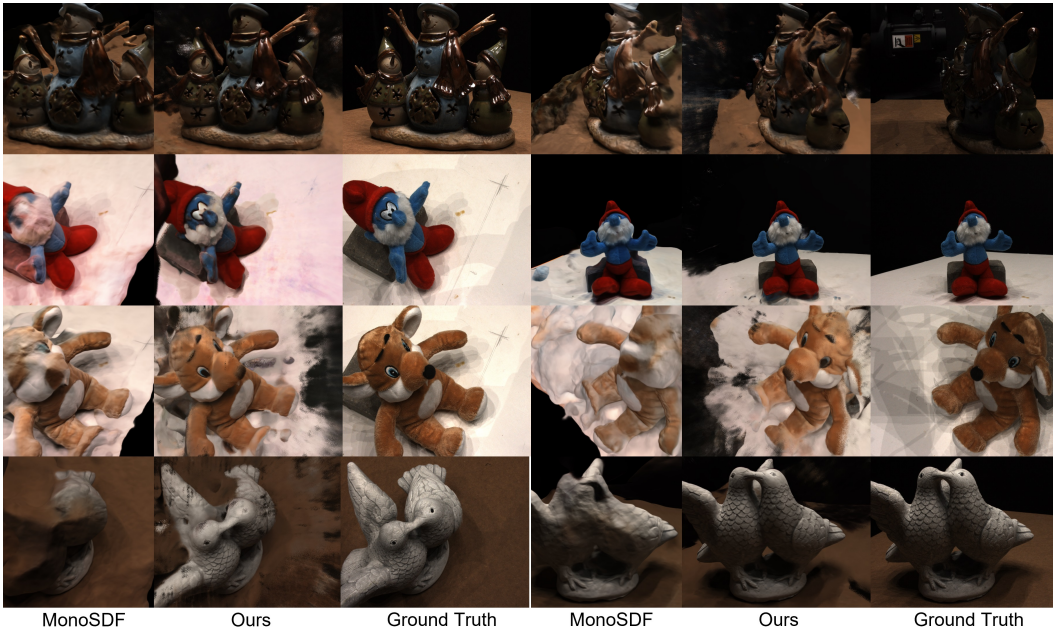


Figure 15: Novel View Synthesis Results on DTU dataset trained using 3 views.

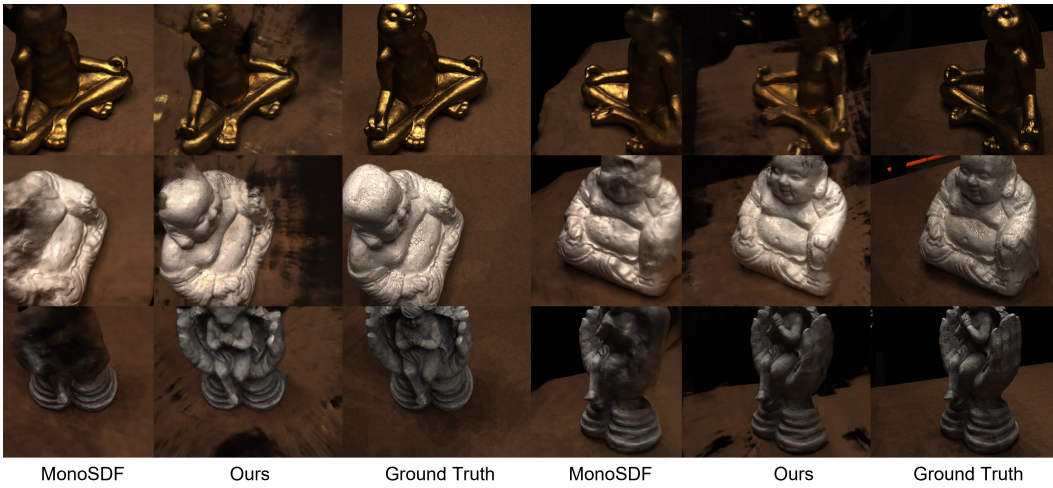


Figure 16: Novel View Synthesis Results on DTU dataset trained using 3 views.

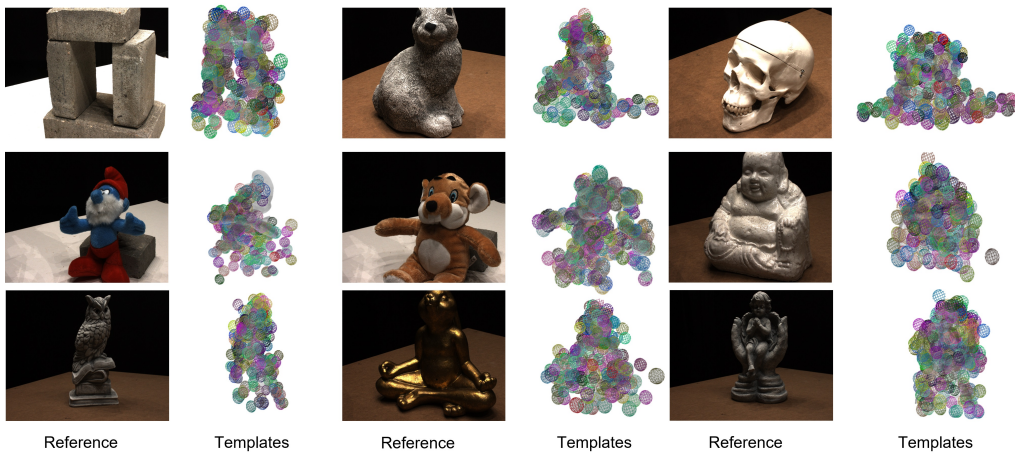


Figure 17: Template predictions on DTU dataset.